SUPPLEMENTARY MATERIAL VOLCANICA

Supplementary Material for: PyIRoGlass: An open-source, Bayesian MCMC algorithm for fitting baselines to FTIR spectra of basaltic-andesitic glasses

Sarah C. Shi *[α], W. Henry Towbin[α], Terry Plank[α], Anna Barth[α,β], Daniel Rasmussen[α,γ], Yves Moussallam[α], Hyun Joo Lee[α], and William Menke[α]

[α]Lamont-Doherty Earth Observatory, Columbia University. New York, NY USA.
[β]University of California, Berkeley. Berkeley, CA USA.
[γ]National Museum of Natural History, Smithsonian Institution. Washington, DC USA.

This supplementary material accompanies the article:

> Shi, S. C., Towbin, W. H., Plank, T., Barth, A., Rasmussen, D., Moussallam, Y., Lee, H. J., and Menke, W. (2024) "PyIRoGlass: An open-source, Bayesian MCMC algorithm for fitting baselines to FTIR spectra of basaltic-andesitic glasses", *Volcanica*, *7*(2), pp. 447–501. DOI: https://doi.org/10.30909/vol.07.02.447501.

Shi et al. (2024) should be cited if this material is used independently of the article.

S1 Data and GitHub/Zenodo overview

S1.1 Data overview

Over 500 transmission FTIR spectra were used to train, validate and test PyIRoGlass. The training dataset is composed of the 55 spectra of glasses with volatiles below detection, analyzed by PCA to determine the fundamental shape and variability of the baseline, contained within the GitHub Baseline_PCA directory. The validation dataset is composed of 97 spectra of melt inclusions from the 2018 eruption of Volcán de Fuego, Guatemala (IGSN: TAP000081), contained within the GitHub Inputs/Transmission_Spectra/Fuego directory. These spectra were first used to examine the performance of the PyIRoGlass fitting routine. The test dataset is composed of 148 spectra of synthetic glasses with devolatilized baselines and synthetic and natural interlaboratory standard glasses, contained within the GitHub Inputs/Transmission_Spectra/Standards directory. The remaining spectra within the directory are the 200 spectra collected for internal check standards acquired while analyzing the Volcán de Fuego melt inclusions.

S1.2 GitHub/Zenodo overview

The directory forest presented provides an overview of the file structure contained within the GitHub and Zenodo. The .py file with code generating each figure within the paper is indicated.

S2 Newtonian inversion

The implicit theory or model is formulated as:

$$f(x) = -y + m_0 + m_1 p = 0, \tag{S1}$$

where m is the vector of coefficients to be solved, p is the predictor variable, y is the dependent variable, and x is vector:

$$x = \left[[y]_N \quad [p]_N \quad [m_0] \quad [m_1] \right], \tag{S2}$$

where N is the length of experimental data. The ordinary least squares solution and covariance matrix to the implicit model is defined as:

$$m_{ls} = (G^T * G)^{-1} (G * y), \tag{S3}$$

and the covariance matrix described by:

$$cov_{ls} = ((G^T * \sigma_y)^{-2} * G)^{-1}, \tag{S4}$$

where G is the data matrix:

$$G = \begin{bmatrix} 1 & p_0 \\ \dots & \dots \\ 1 & p_N \end{bmatrix} \tag{S5}$$

The x_i matrix is defined by the measured data and the ordinary least squares solution. The least squares covariance matrix accounts for uncertainty in dependent variable y but not in predictor or compositional parameter p. We thus move to iteratively solve for m and c to account for these uncertainties. Uncertainties in dependent variable y and compositional parameter p can be applied with a diagonal covariance matrix:

$$cov_x = \begin{bmatrix} [\sigma_y^2] & & & \\ & [\sigma_p^2] & & \\ & & [cov_{ls,m_0}] & \\ & & & [cov_{ls,m_1}] \end{bmatrix} \tag{S6}$$

We successively solve for the m vector, and thus the x matrix with the implicit Newtonian algorithm:

$$x_n = x_i + MO * (F * (x_{n-1} - x)) \tag{S7}$$

where x_n is the matrix at iteration n, x_{n-1} is the matrix at the previous iteration, x_i is the initial matrix, f_{n-1} is the model at

* sarah.shi@columbia.edu

Editor: K. Iacovino | Typesetter: J. Farquharson

PyIRoGlass
- Baseline_Comparison
  - BaselineComp.py – Generates Figure 11
  - DetectionLimit.py – Generates Figure 14
  - PeakHeightComp.py – Generates Figures 12 and 15
- Baseline_PCA
  - BaselinePC_Generate.py – Generates baseline principal components
  - H2OmPC_Generate.py – Generates H_2O_m peak principal components
  - BaselinePCA_Vis.py – Generates Figures 2 and 3 and 4
- Epsilon_Inversion
  - Epsilon_Comp_Regress.py – Generates Figure 5
  - Epsilon_PHArea_Regress.py – Generates Supplement Figures 1 and 2
- FINALDATA – Results from PyIRoGlass
- Inputs – Input spectra and thickness chemistry files
  - ReflectanceSpectra – Reflectance FTIR spectra
  - TransmissionSpectra – Transmission FTIR spectra
    - Fuego
    - Standards
- Peak_Fit
  - PeakFitPlotting.py – Generates Figures 1 and 9
- Thickness
  - ThicknessFuntion.py – Generates Figures 6 and 7
- Unit_Tests – All pytest unit tests
  - test_concentration.py
  - test_density_epsilon.py
  - test_fittingfunc.py
  - test_inversion.py
  - test_loading.py
  - test_plotting.py
  - test_thickness.py
- Volatiles_Speciation
  - StandardsPlot.py – Generates Figure 13
  - SpeciationPlot.py – Generates Figure 10
- docs – Documentation for ReadtheDocs
- src/PyIRoGlass – Source code for PyPI
  - BaselineAvgPC.npz – Baseline principal components
  - H2Om1635PC.npz – H_2O_m peak principal components
  - __init__.py – Initializes package for PyIRoGlass
  - _version.py – States version for PyPI
  - core.py – Core code for PyIRoGlass
  - inversion.py – Inversion code for PyIRoGlass
  - thickness.py – Thickness code for PyIRoGlass
- .readthedocs.yaml – ReadtheDocs configuration file
- LICENSE.txt – GNU GPLv3
- PyIRoGlass_Run.py – Example run file generating Figure 8
- PyIRoGlass_Run_colab.py – Example run file
- README.md – README file with key information on PyIRoGlass
- environment.yml – YML file with Python environment information
- setup.cfg – Setup information for PyIRoGlass
- setup.py – Setup information for PyIRoGlass

the previous iteration, and F is the diagonal gradient matrix (matrix of derivatives of implicit theory f with respect to each component of matrix x) and MO is the Lagrange multiplier.

In some instances, as in Section S2.1, a fit in which the intercept value is forced to zero may be warranted. This result can be achieved by setting the prior value of the intercept [m_0]=0 in Equation S2 and the corresponding prior covariance [cov_{ls,m_0}]=^{2} in Equation S6, where ≪1.

Two forms of error—the error of calibration and the error of a single application of the inversion to melt composition—can be quantified. The 95% confidence interval of the error of calibration is two times the posterior covariance in y, between the predicted y of the model (varying within error) and the experimental y. The 95% confidence interval of a single application of the model incorporates the error of calibration as well as analytical uncertainty of compositional parameter derivation, applied with:

$$c_T = Zc_mZ^T + mc_zm^T, \quad \text{(S8)}$$

where Z is a vertical matrix of the measured compositional parameter, c_m is the diagonal posterior covariance on the model parameter coefficients, m is the vertical matrix of the posterior model parameter coefficients, and c_z is a diagonal matrix of the uncertainty of measured compositional parameter. Results from the inversion are presented in Table S2 and Table S3, with all data inputs and code in the GitHub Epsilon_Inversion directory.

S2.1 Inversion for ND70-Series Linear and Integrated Molar Absorptivity

We determine linear molar absorptivity (ε) and integrated molar absorptivity (ε_i) for a suite of basaltic reference materials of ND70 (Table 3 and Table 4 in paper) independently analyzed in a study from Moussallam et al. [2024]. The ND70 basaltic glass reference materials were synthesized from a natural back-arc basin basalt composition, loaded with variable concentrations of H_2O, CO_2, S, Cl, and F, in piston cylinder experiments at the Lamont-Doherty Earth Observatory (LDEO) and characterized with numerous analytical techniques. Absolute concentrations of H_2O and CO_2 were determined with the ion beam analysis techniques of Elastic Recoil Detection Analysis (ERDA) for H_2O and Nuclear Reaction Analysis (NRA) for CO_2 at Laboratoire d'Etude des Eléments Légers (LEEL) joint CEA-CNRS laboratory at Université Paris-Saclay. Further analyses were performed by Secondary Ion Mass Spectrometry (SIMS) for H_2O, CO_2, S, Cl, and F at Centre de Recherches Pétrographiques et Géochimiques, Université de Lorraine (Nancy).

Calibration of the linear and integrated molar absorptivities for the $H_2O_{t,3550}$ and CO_3^{2-} peaks rely on five of the ND70 reference materials, analyzed for H_2O by ERDA and CO_2 by NRA at LEEL, for H_2O with Cs^+ beam by SIMS at Nancy, and for H_2O and CO_2 by FTIR at LDEO (Table S1). The mean H_2O concentration was calculated by combining data from both ERDA and SIMS analyses to provide an aggregated view of concentration and to minimize uncertainty. The CO_2 concentrations by NRA were acquired during the same analytical session. Mean peak heights and peak areas acquired by FTIR were calculated with PyIRoGlass from replicate analyses of the reference materials, with samples saturated in $H_2O_{t,3550}$ excluded. Peak heights for the $H_2O_{t,3550}$ peak are determined from the mean and standard deviation on three repeat fittings of the asymmetric least squares baseline. Peak areas for the $H_2O_{t,3550}$ peak were determined by using the SciPy implementation of Simpson's Rule to integrate beneath the asymmetric least squares baseline-subtracted peak [Eilers 2004; Virtanen et al. 2020]. Peak heights for the CO_3^{2-} peak are determined from the PyIRoGlass best-fit parameters. Both the $CO_{3,1515}^{2-}$ and $CO_{3,1430}^{2-}$ peaks are considered, given that the contribution of the $H_2O_{m,1635}$ is accounted for by PyIRoGlass. This is a development from previous calibrations from Botcharnikov et al. [2006], Behrens et al. [2009], and Shishkina et al. [2014]. The $CO_{3,1515}^{2-}$ and $CO_{3,1430}^{2-}$ peaks yield individual molar absorptivities that are within 2% of each other, so are aggregated in the calibration. Peak areas for the CO_3^{2-} peak are calculated from these parameters as:

$$A_i = a\sqrt{2\pi\sigma^2}, \quad \text{(S9)}$$

where A_i is the area, a is the peak amplitude, and σ is the peak half-width. To determine ε and ε_i, the knowns from the Beer-Lambert Law (y in Equation S1) are regressed against the known concentration from independent analytical methods (p in Equation S1, the average of ERDA/SIMS concentrations for H_2O and the NRA concentration for CO_2). The uncertainty in the knowns from the Beer-Lambert Law (σ_y in Equation S6) propagates uncertainties in peak height or area, density, and thickness; the uncertainty in the known concentrations from independent analytical methods (σ_p in Equation S6) propagates uncertainties from repeat analyses and calibration. ε or ε_i can thus be determined from the slope of the relationship, when the intercept is forced to pass through zero. This is done by setting the prior value of the intercept [m_0]=0 in Equation S2 and the corresponding prior covariance [cov_{ls,m_0}]=^{2} in Equation S6, where ≪1. The inversion inputs are provided in Table S1 and the resultant ε and ε_i values are provided in Table S2. The ND70 basalt composition with τ=0.646 and =0.236 returns $\varepsilon_{H_2O_{t,3550}}$=63.03±4.47 L/mol·cm, $\varepsilon_{CO_{3,1515,1430}^{2-}}$=303.44±9.20 L/mol·cm, $\varepsilon_{i,H_2O_{t,3550}}$=31906±1503 L/mol·cm^2, and $\varepsilon_{i,CO_{3,1515,1430}^{2-}}$=25001±756 L/mol·cm^2.

S2.2 Inversion for composition-dependent molar absorptivity

We determine the relationships between $\varepsilon H_2O_{m,5200}$, εOH^-_{4500}, $\varepsilon H_2O_{t,3550}$, $\varepsilon H_2O_{m,1635}$, and εCO_3^{2-} and their corresponding compositional parameters using a Newtonian inversion technique for data published between 1982 and 2024. In the full dataset, τ spans the range of 0.50-0.90 and spans 0.23-0.84. To determine this relationship, molar absorptivities (ε, y in Equation S1) are regressed against the compositional parameters (τ or , p in Equation S1), We assume an uncertainty of 10% for $\varepsilon H_2O_{m,5200}$, $\varepsilon H_2O_{t,3550}$, $\varepsilon H_2O_{m,1635}$, εCO_3^{2-}, and assume an uncertainty of 20% for εOH^-_{4500} — or the σ_y in Equation S6 — given increased uncertainties on baselines with linear and Gaussian fits to the peak. We assign a 2.5% uncertainty to the compositional parameters (σ_p in Equation S6), based on the propagated uncertainties in calculating cation

Table S1: Inversion inputs for calibrating basalt ND70-Series linear molar absorptivities (ε) and integrated molar absorptivities (ε_i). H_2O concentrations are the mean of ERDA/SIMS analyses, and CO_2 concentrations are from NRA. A is absorbance intensity, A_i is integrated absorbance. Density is calculated by PyIRoGlass with the Lesher and Spera [2015] calibration. Thickness is determined by micrometer and/or the reflectance FTIR spectrum method.

Sample	H_2O (wt.%)	H_2O (wt.%)	n	$A_{H_2O_{t,3550}}$	$A_{i,H_2O_{t,3550}}$	Density ($kg{\cdot}m^{-3}$)	Thickness (μm)
ND70-2-01	2.37	0.24	3	3.23	1568	2812	120
ND70-3-01	2.92	0.31	4	1.00	552	2754	27
ND70-3-01	2.92	0.31	1	2.69	1627	2798	112
ND70-4-02	3.68	0.35	5	1.94	1004	2728	44
ND70-5-02	4.96	0.52	6	0.65	354	2709	14
ND70-6-02	6.32	0.61	3	1.35	684	2691	25

Sample	CO_2 (ppm)	CO_2 (ppm)	n	$A_{CO_{3,1515}^{2-}}$	$A_{CO_{1430}^{2-}}$	$A_{i,CO_{3,1515}^{2-}}$	$A_{i,CO_{3,1430}^{2-}}$	Density ($kg{\cdot}m^{-3}$)	Thickness (μm)
ND70-2-01	1837	35	3	0.36	0.36	28.33	33.54	2812	120
ND70-3-01	2689	54	4	0.14	0.13	10.64	11.79	2754	27
ND70-3-01	2689	54	3	0.50	0.48	38.86	42.52	2796	112
ND70-4-02	4122	65	5	0.43	0.41	33.87	35.85	2728	44
ND70-4-02	4122	65	3	0.87	0.84	67.66	74.37	2770	115
ND70-5-02	12682	105	6	0.35	0.34	27.76	29.68	2709	14
ND70-6-02	16847	120	3	0.83	0.87	69.32	68.05	2691	25

Table S2: Linear molar absorptivity (ε) and integrated molar absorptivity (ε_i) Newtonian inversion best-fit parameters and uncertainties. The slope m_1 and associated uncertainty σm_1 capture the ε or ε_i for the ND70 basalt with $\tau = 0.646$ and $\eta = 0.236$. The intercept m_0 and σm_0 are zero, as the intercept is forced through zero.

	m_0	σm_0	m_1	σm_1
$\varepsilon_{H_2O_{t,3550}}$	0	0	63.03	4.47
$\varepsilon_{CO_{3,1515,1430}^{2-}}$	0	0	303.44	9.20
$\varepsilon_{i,H_2O_{t,3550}}$	0	0	31906	1503
$\varepsilon_{i,CO_{3,1515,1430}^{2-}}$	0	0	25001	756

fractions from the oldest study with reported electron microprobe uncertainties. The resultant compositionally-dependent ε calibration is provided in Table S3 and presented in Figure 5 in the paper.

Table S3: ε Newtonian inversion best-fit parameters, uncertainties on best-fit parameters, and associated covariance matrices.

	m_0	σm_0	m_1	σm_1
$\varepsilon_{H_2O_{m,5200}}$	−2.291	0.113	4.676	0.166
$\varepsilon_{OH_{4500}^-}$	−1.633	0.181	3.533	0.266
$\varepsilon_{H_2O_{t,3550}}$	15.737	6.169	71.397	8.797
$\varepsilon_{H_2O_{m,1635}}$	−50.398	4.566	124.251	6.276
$\varepsilon_{CO_{3,1515,1430}^{2-}}$	417.174	9.211	−318.094	18.429

S3 Analytical Methodology

S3.1 Transmission Fourier Transform Infrared Spectroscopy (FTIR)

FTIR data of melt inclusions (MIs) from the 2018 eruption of Volcán de Fuego, Guatemala are reported here as exemplar and test data (and are the topic of a broader project reported in Shi et al. [2021]). Olivine hosted MIs were selected on four primary criteria: euhedral to subhedral crystal habit, lack of cracks, presence of volcanic glass to ensure the preservation of true crystal rims, and presence of glassy MIs (>50 μm in diameter to accommodate the FTIR aperture). Selected olivine crystals were visually oriented (and the habit confirmed with EBSD), mounted, and polished to intersect the MI within the exposed (010) plane while maximizing wafer thickness. Singly-polished olivine crystals were flipped over to ensure that the polished (010) plane lay flat on the one-inch glass round. Crystals were polished to intersect the other side of the MI on the a-c plane, yielding doubly-polished and oriented olivine wafers. All doubly-polished olivine wafers were

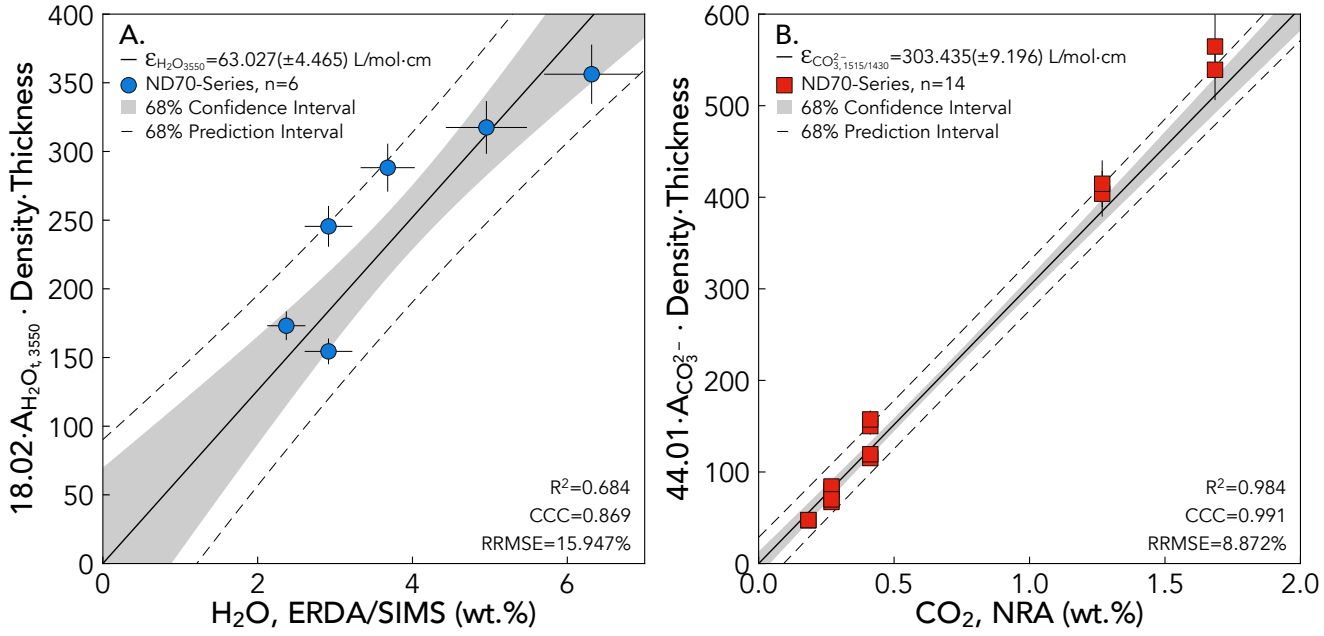

Figure S1: Linear molar absorptivity (ε) inversion results for ND70-Series basalt (τ=0.646, =0.236), with $H_2O = 2.37 - 6.32$wt.% and $CO_2 = 0.18 - 1.68$ wt.%. Calibration data presented in Table S1. Slope m_1 and associated uncertainty σm_1 in the determined ε. Intercept m_0 and σm_0 are zero. [A] $\varepsilon_{H_2O_{t,3550}} = 63.03 \pm 4.47 \mathrm{L/mol \cdot cm}$, with a coefficient of determination of 0.684. The inversion is more uncertain than that of CO_3^{2-}, given larger H_2O concentration uncertainties. [B] $\varepsilon_{CO_{3,1515,1430}^{2-}} = 303.44 \pm 9.20 \mathrm{L/mol \cdot cm}$, with a coefficient of determination of 0.984. The calibration is tightly constrained given the lower CO_2 concentration uncertainties.

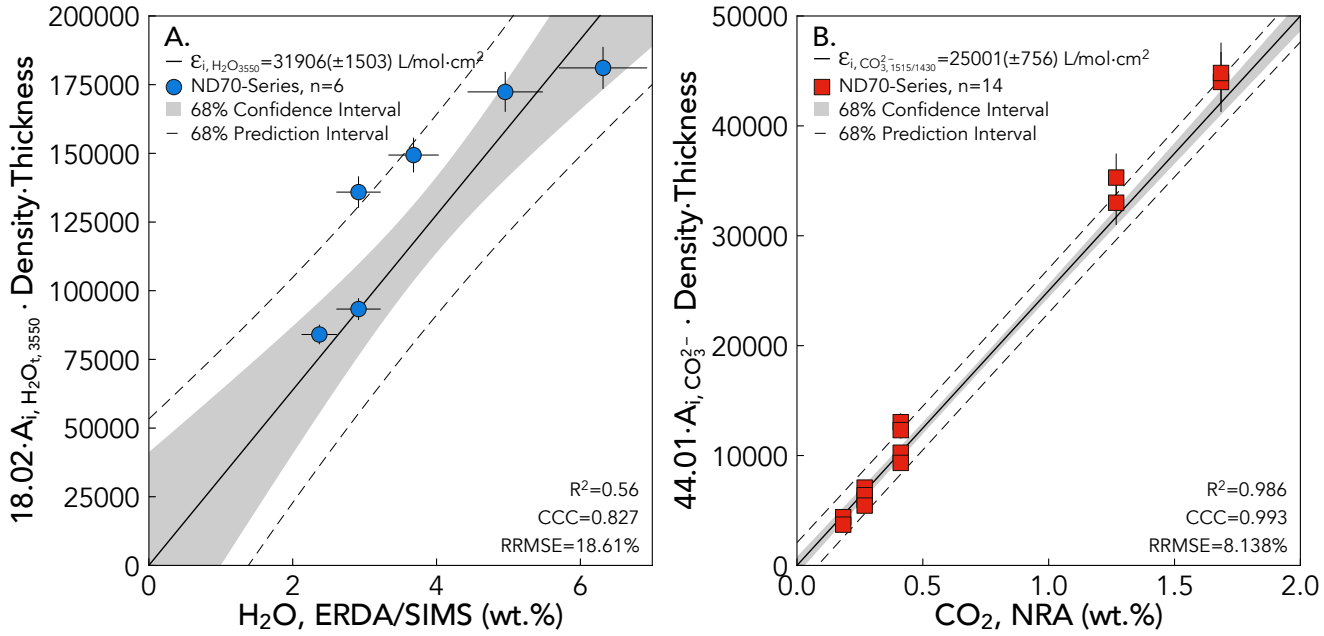

Figure S2: Integrated molar absorptivity (ε_i) inversion results for ND70-Series basalt ($\tau = 0.646$, $\eta = 0.236$), with $H_2O = 2.37 - 6.32$wt.% and $CO_2 = 0.18 - 1.68$wt.%. Calibration data presented in Table S1. Slope m_1 and associated uncertainty σm_1 in the determined ε_i. Intercept m_0 and σm_0 are zero. [A] $\varepsilon_{i,H_2O_{t,3550}} = 31906 \pm 1503 \mathrm{L/mol \cdot cm^2}$, with a coefficient of determination of 0.560 which is lower than that of the $\varepsilon_{H_2O_{t,3550}}$ inversion. Scatter may be larger with peak areas for the $H_2O_{t,3550}$ peak [Ohlhorst et al. 2001]. [B] $\varepsilon_{i,CO_{3,1515,1430}^{2-}} = 25001 \pm 756 \mathrm{L/mol \cdot cm^2}$, with a coefficient of determination of 0.984 which is slightly higher than that of $\varepsilon_{CO_{3,1515,1430}^{2-}}$. Scatter may be smaller with peak areas for the CO_3^{2-} peaks. Exploring integrated molar absorptivities may be a promising future avenue for investigation.

removed from Crystalbond and cleaned with a ten minute ultrasonication in acetone prior to FTIR analysis.

Natural glass standards and olivine-hosted MIs were analyzed with the Thermo Scientific Nicolet iN10 MX Fourier Transform Infrared (FTIR) Spectrometer at the Lamont-Doherty Earth Observatory. Dry and CO_2-scrubbed air purged the machine and measurements were made on a liquid nitrogen-cooled MCT-A detector. Glass standards and MIs were placed on a CaF_2 plate within the sample holder for measurement of IR absorbance during transmission in the detector spectral range of 8000-450 wavenumbers (cm^{-1}). The FTIR was purged for twenty minutes to decrease the signal of atmospheric H_2O and CO_2. Glasses and melt inclusions were mapped for absorbance to determine potential heterogeneity in volatile concentrations and to determine the boundaries of measurement—particularly for MI to ensure double intersection. Absorbance maps were generated at a point spacing of 10×10 µm, with 16 scans taken at each point at a resolution of 16 cm^{-1}. The relatively few scans and low resolution were balanced to yield manageable mapping times of approximately 15 minutes for each MI. Maps guided the selection of optimal regions for volatile analyses. Three repeat measurements were collected for each glass standard or MI, with 256 collection scans at 4 cm^{-1} spectral resolution. Background scans were collected under the same conditions through the CaF_2 plate. Aperture sizes (30-200 µm for glass standards and 15-50 µm for MIs) were selected to maximize analytical area and to ensure that light propagated solely through the MI without including the host olivine. The Happ-Genzel apodization function within the Thermo-Nicolet OMNIC Picta software was applied to each spectrum to maintain resolution and reduce noise. Three repeat measurements were taken for each MI. Internal standards of back-arc basin glass D1010 analyzed by Newman et al. 2000 with FTIR and basaltic melt inclusions CN-C-OL1', CN92C-OL2, and ETF46 analyzed by Barth et al. 2019 and Barth 2021 with SIMS were measured at the beginning and end of each analytical session as internal check standards.

S3.2 Reflectance Fourier Transform Infrared Spectroscopy (FTIR)

Three repeat thickness measurements of olivine-hosted melt inclusions were acquired using a Mitutoyo 543-783B Digimatic Indicator, as well as with the reflectance method described by Nichols and Wysoczanski 2007 implemented in PyIRoGlass. Two reflectance spectra were taken adjacent to olivine-hosted melt inclusions with 256 collection scans at 4 cm^{-1} spectral resolution, with aperture sizes of 50×50 µm. Background scans were collected under the same conditions on a highly reflective gold plate with a reflectance coefficient of unity [Nichols and Wysoczanski 2007]. The basaltic glass refractive index is quantified to be 1.546 [Kumagai and Kaneoka 2003]. The rhyolitic glass refractive index is not as well quantified, showing additional variability and spanning the range of $1.48<n<1.51$ [Tröger et al. 1959; Tamic et al. 2001]. Refractive indices for glasses of variable composition can be calibrated with the digital micrometer [Tamic et al. 2001; Duncan and Dasgupta 2015]. The olivine mean refractive index, averaged across the three crystallographic axes, is described by forsterite content with linear relationships described in Howie et al. 1992.

S3.3 Electron Probe Microanalyzer (EPMA)

Major and trace elements in glass and olivine were analyzed by wavelength dispersive X-ray spectroscopy with the Cameca SXFive-TACTIS electron microprobe (EPMA) at the American Museum of Natural History. Calibration was completed with natural and synthetic mineral and oxide standards. Glasses were measured with an accelerating voltage of 15 keV, variable working current of 4 nA, 10 nA, and 40 nA, and spot size of 1 µm. Sulfur was measured on the sulfate peak position and was standardized on $BaSO_4$. Duplicate MI analyses were collected proximal to the center of the inclusion. Olivines were measured with an accelerating voltage of 15 keV, variable working current of 10 nA and 300 nA, and spot size of 1 µm. Duplicate olivine-host analyses were collected approximately 15 µm from the MI.

Replicate analyses of the check standard MR:ND-70-01 and secondary standard San Carlos Olivine were performed every 10 analyses. Column conditions and additional assessments of instrumental drift, precision, and accuracy from analysis of standard analyses are quantified in Table S4 and Table S5. Analytical precision is quantified as the relative standard deviation (standard deviation of repeat analysis / mean composition of standard during session) of repeated analyses of a secondary standard during an analytical session. Analytical accuracy is quantified as the relative difference in mean composition of the secondary standard during an analytical session divided by the published value for the standard ((analytical mean - published mean) / published mean). Published concentrations for MR:ND-70-01 are from Ruprecht and Plank [2013] and for San Carlos Olivine are from Lloyd et al. [2013]. Specific acquisition parameters and assessments of analytical precision and accuracy are presented in the following tables.

Copyright

References

Barth, A. (2021). "Ascent rates and volatiles of explosive basaltic volcanism". PhD thesis. Columbia University in the City of New York. DOI: 10.7916/d8-zkzt-a130.

Barth, A., M. Newcombe, T. Plank, H. Gonnermann, S. Hajimirza, G. J. Soto, A. Saballos, and E. Hauri (2019). "Magma decompression rate correlates with explosivity at basaltic volcanoes—Constraints from water diffusion in olivine". In: *Journal of Volcanology and Geothermal Research* 387, page 106664. DOI: 10.1016/j.jvolgeores.2019.106664.

Table S4: Assessment of EPMA analytical conditions, precision, and accuracy for glass analyses.

Element	Spectrometer	Crystal	Peak Location	Current (nA)	Peak Count Time (s)	Background Count Time (s)	Calibration Material	Precision (%)	Accuracy (%)
F	Sp4	TAP	71277	4	30	15	MgF_2	-	-
Na	Sp2	LTAP	46352	4	2	20	Albite	14.53	6.64
Mg	Sp2	LTAP	38469	10	30	15	Wakefield Diopside	0.35	2.11
Al	Sp2	LTAP	32443	10	30	15	Albite	2.17	0.76
Si	Sp4	TAP	27760	10	30	15	Wakefield Diopside	1.11	-1.47
P	Sp1	PET	70287	10	30	15	Berlinite	23.07	16.22
K	Sp3	LPET	42821	10	30	15	Ortho_1	1.48	2.13
Ca	Sp1	PET	38314	10	30	15	Wakefield Diopside	1.19	0.15
Ti	Sp3	LPET	31457	10	30	15	Rutile	3.49	-0.28
Mn	Sp5	LLIF	52207	10	30	15	Rhodon	14.53	-4.04
Fe	Sp5	LLIF	48101	10	20	15	RKFAYb7	0.66	-1.50
S	Sp3	LPET	61472	40	30	15	Barite	3.04	37.88
Cl	Sp1	PET	53959	40	30	15	Scapolite	31.28	4.48

Table S5: Assessment of EPMA analytical conditions, precision, and accuracy for olivine analyses.

Element	Spectrometer	Crystal	Peak Location	Current (nA)	Peak Count Time (s)	Background Count Time (s)	Calibration Material	Precision (%)	Accuracy (%)
Mg	Sp2	LTAP	38517	10	20	10	San Carlos Olivine	0.57	0.00
Si	Sp4	TAP	27740	10	20	10	San Carlos Olivine	0.60	-0.86
Fe	Sp5	LLIF	48081	10	20	10	Fayalite B6	1.05	1.23
Al	Sp2	LTAP	32477	300	90	45	Anorthite	4.68	28.61
P	Sp3	LPET	70319	300	40	20	Apatite	30.37	135.28
Ca	Sp1	PET	38388	300	35	17.5	Anorthite	3.77	-9.14
Ti	Sp3	LPET	31401	300	40	20	Rutile_6	18.28	220.68
Cr	Sp1	PET	26156	300	40	20	$MgCr_2O_4$	16.78	53.85
Mn	Sp5	LLIF	52191	300	30	15	Rhodonite	2.36	1.76
Ni	Sp5	LLIF	41173	300	40	20	Diopside_Ni	3.59	26.53

Behrens, H., V. Misiti, C. Freda, F. Vetere, R. E. Botcharnikov, and P. Scarlato (2009). "Solubility of H_2O and CO_2 in ultrapotassic melts at 1200 and 1250°C and pressure from 50 to 500 MPa". In: *American Mineralogist* 94(1), pages 105–120. DOI: 10.2138/am.2009.2796.

Botcharnikov, R. E., H. Behrens, and F. Holtz (2006). "Solubility and speciation of C–O–H fluids in andesitic melt at T= 1100–1300 C and P= 200 and 500 MPa". In: *Chemical Geology* 229(1-3), pages 125–143. DOI: 10.1016/j.chemgeo.2006.01.016.

Duncan, M. S. and R. Dasgupta (2015). "Pressure and temperature dependence of CO_2 solubility in hydrous rhyolitic melt: implications for carbon transfer to mantle source of volcanic arcs via partial melt of subducting crustal lithologies". In: *Contributions to Mineralogy and Petrology* 169(6), pages 1–19. DOI: 10.1007/s00410-015-1144-5.

Eilers, P. H. (2004). "Parametric time warping". In: *Analytical Chemistry* 76(2), pages 404–411. DOI: 10.1021/ac034800e.

Howie, R., J. Zussman, and W. Deer (1992). *An introduction to the rock-forming minerals*. Longman London, UK. DOI: 10.1180/DHZ.

Kumagai, H. and I. Kaneoka (2003). "Relationship between submarine MORB glass textures and atmospheric component of MORBs". In: *Chemical Geology* 200(1-2), pages 1–24. DOI: 10.1016/S0009-2541(03)00077-9.

Lesher, C. E. and F. J. Spera (2015). "Thermodynamic and transport properties of silicate melts and magma". In: *The Encyclopedia of Volcanoes*. Elsevier, pages 113–141. DOI: 10.1016/B978-0-12-385938-9.00005-5.

Lloyd, A. S., T. Plank, P. Ruprecht, E. H. Hauri, and W. Rose (2013). "Volatile loss from melt inclusions in pyroclasts of differing sizes". In: *Contributions to Mineralogy and Petrol-*

Table S6: Calibration materials at the American Museum of Natural History (AMNH). Compositions presented in %.

Calibration Material	Si	Ti	Al	Fe	Mn	Mg	Ca	Na	K	P	Cr	Ni	S	Ba	F	Cl	O
MgF_2						39.01									60.99		
Albite	32.13		10.29					8.77									48.81
Wakefield Diopside	25.94	0.02	0.02	0.09	0.02	11.22	18.53	0.02									44.43
Berlinite			22.12							25.40							52.48
Ortho_1	30.10		9.83					0.85	12.39					0.7			45.94
Rutile_6		59.95															40.05
Rhodonite	21.98			1.80	35.01	2.36	1.06										37.73
RKFAYb7	13.84		0.05	52.62	1.55	0.06	0.02										31.37
Barite													13.74	58.84			27.42
Scapolite	25.35		12.33				6.52	5.63	1.40					2.74			45.70
San Carlos Olivine	19.08			7.42	0.11	29.80	0.02					0.29					43.28
Fayalite B6	13.66	0.02		52.51	1.66												31.78
Anorthite	20.61	0.01	18.77	0.36		0.05	13.9	0.3		0.01				0.01			45.98
Apatite	0.12		0.01	0.05			39.27	0.18		17.77			0.24		3.4		39.27
$MgCr_2O_4$	12.64										54.08						33.28
Diopside_Ni	24.91		0.45	0.12		8.62	17.87					5.06					43.01

ogy 165, pages 129–153. DOI: 10.1007/s00410-012-0800-2.

Moussallam, Y., W. Tobbin, T. Plank, H. Bureau, H. Khodja, Y. Guan, C. Ma, M. B. Baker, E. M. Stolper, F. U. Naab, B. D. Monteleone, G. A. Gaetani, K. Shimizu, U. Takayuki, H. J. Lee, S. Ding, S. C. Shi, and E. F. Rose-Koga (2024). "ND70 series basaltic glass reference materials for volatile element (H_2O, CO_2, S, Cl, F) analysis and the C ionisation efficiency suppression effect of water in silicate glasses in SIMS analysis". In: *Geostandards and Geoanalytical Research*. DOI: 10.31223/X5QQ4P.

Newman, S., E. Stolper, and R. Stern (2000). "H_2O and CO_2 in magmas from the Mariana arc and back arc systems". In: *Geochemistry, Geophysics, Geosystems* 1(5). DOI: 10.1029/1999GC000027.

Nichols, A. R. and R. Wysoczanski (2007). "Using micro-FTIR spectroscopy to measure volatile contents in small and unexposed inclusions hosted in olivine crystals". In: *Chemical Geology* 242(3-4), pages 371–384. DOI: 10.1016/j.chemgeo.2007.04.007.

Ohlhorst, S., H. Behrens, and F. Holtz (2001). "Compositional dependence of molar absorptivities of near-infrared OH- and H_2O bands in rhyolitic to basaltic glasses". In: *Chemical Geology* 174(1-3), pages 5–20. DOI: 10.1016/S0009-2541(00)00303-X.

Ruprecht, P. and T. A. Plank (2013). "Feeding andesitic eruptions with a high-speed connection from the mantle". In: *Nature* 500(7460), pages 68–72. DOI: 10.1038/nature12342.

Shi, S., A. Barth, T. Plank, W. Tobbin, O. Flores, and C. Arias (2021). "Magma stalling weakens eruption". In: *AGU Fall Meeting Abstracts*. Volume 2021, V25E–09.

Shishkina, T. A., R. E. Botcharnikov, F. Holtz, R. R. Almeev, A. M. Jazwa, and A. A. Jakubiak (2014). "Compositional and pressure effects on the solubility of H_2O and CO_2 in mafic melts". In: *Chemical Geology* 388, pages 112–129. DOI: 10.1016/j.chemgeo.2014.09.001.

Tamic, N., H. Behrens, and F. Holtz (2001). "The solubility of H_2O and CO_2 in rhyolitic melts in equilibrium with a mixed CO_2–H_2O fluid phase". In: *Chemical Geology* 174(1-3), pages 333–347. DOI: 10.1016/S0009-2541(00)00324-7.

Tröger, W. E., H. U. Bambauer, F. Taborszky, and H.-D. Trochim (1959). *Optische Bestimmung der gesteinsbildenden Minerale-Teil I.: Bestimmungstabellen*. Schweizerbart'sche Verlagsbuchhandlung.

Virtanen, P., R. Gommers, T. E. Oliphant, M. Haberland, T. Reddy, D. Cournapeau, E. Burovski, P. Peterson, W. Weckesser, J. Bright, S. J. van der Walt, M. Brett, J. Wilson, K. J. Millman, N. Mayorov, A. R. J. Nelson, E. Jones, R. Kern, E. Larson, C. J. Carey, İ. Polat, Y. Feng, E. W. Moore, J. VanderPlas, D. Laxalde, J. Perktold, R. Cimrman, I. Henriksen, E. A. Quintero, C. R. Harris, A. M. Archibald, A. H. Ribeiro, F. Pedregosa, P. van Mulbregt, and SciPy 1.0 Contributors (2020). "SciPy 1.0: Fundamental Algorithms for Scientific Computing in Python". In: *Nature Methods* 17, pages 261–272. DOI: 10.1038/s41592-019-0686-2.